Laser-Induced Shock Compression of Copper: Orientation and Pressure Decay Effects

M.S. SCHNEIDER, B.K. KAD, F. GREGORI, D. KALANTAR, B.A. REMINGTON, and M.A. MEYERS

Pure copper monocrystals with [001] and [$\bar{1}$34] orientations were subjected to ultrashort shock pulses ranging in initial duration from 2.5 to 10 ns, induced by a laser at energies ranging from 10 to 70 MJ/m^2. The deformation structure was significantly dependent on the crystallographic orientation and depth from the laser-impacted surface, as characterized by transmission electron microscopy (TEM). The threshold pressure for twinning in the [001] direction was observed to be in the range of 20 to 40 GPa compared with 40 to 60 GPa for the [$\bar{1}$34] orientation. Dislocation densities were also different for the two orientations, under similar shock conditions. The [$\bar{1}$34] dislocation density was systematically lower. This is attributed to the activation of fewer slip systems resulting in a lower rate of hardening. The different results found for [001] and [$\bar{1}$34] copper single crystals are described and effects of pressure decay in [$\bar{1}$34] specimens are discussed. Differences in the mechanical response between the two orientations are responsible for differences in the shear stress in the specimens at the imposed pressures and associated strains. The [$\bar{1}$34] orientation is initially subjected to deformation by single slip, (111)[$\bar{1}$01], which has a Schmid factor of 0.4711 and a well-defined easy glide region followed by a cross-slip regime with secondary slip. The [001] orientation has eight slip systems {111}<110> with identical Schmid factors of 0.4082, which lead to immediate work hardening. At an imposed and prescribed pressure (that establishes the strain), the [$\bar{1}$34] orientation exhibits a lower shear stress. The orientation dependence of the twinning stress is much lower, as expressed by Schmid factors. This higher stress for [001] predisposes the onset of twinning in this orientation. The results are interpreted in terms of a criterion in which slip and twinning are considered as competing mechanisms. A constitutive description using a modified mechanical threshold stress (MTS) model is applied to the two orientations, incorporating both slip and twinning. The threshold pressure for twinning is calculated, considering the effect of shock heating. The constitutive description provides a rationale for the experimental results: the calculated thresholds are 17 GPa for [001] and 25 GPa for [$\bar{1}$34].

I. INTRODUCTION

THE effects of shock waves on metals have been studied for over 50 years;[1] most of the experiments used explosives and flyer plates as the means of creating the compression pulse. The short duration of the shock pulse (0.2 to 2 μs) renders direct measurements such as with transmission electron microscopy (TEM) very difficult, and the mechanisms of plastic deformation have to be inferred from postshock examination of the residual defect substructure. It is only recently[2,3,4] that pulsed X-ray diffraction has been used to obtain quantitative information of the lattice distortions at the shock front. These measurements can be used to resolve issues of dislocation generation and motion as well as lattice distortions at the shock front.

M.S. SCHNEIDER, Graduate Student, B.K. KAD, Research Scientist, and M.A. MEYERS, Professor, are with the Department of Mechanical and Aerospace Engineering, University of California, San Diego, La Jolla, CA 92093-0411. Contact e-mail: mameyers@ucsd.edu and m1schneider@ucsd.edu F. GREGORI, Assistant Professor, is with the University of Paris 13, Villetaneuse, France. D. KALANTAR and B.A. REMINGTON, Research Scientists, are with the Lawrence Livermore National Laboratory, Livermore, CA 94550.

This article is based on a presentation given in the symposium "Dynamic Deformation: Constitutive Modeling, Grain Size, and Other Effects: In Honor of Prof. Ronald W. Armstrong," March 2-6, 2003, at the 2003 TMS/ASM Annual Meeting, San Diego, California, under the auspices of the TMS/ASM Joint Mechanical Behavior of Materials Committee.

Recent experiments by Meyers *et al.*[5,6] using [001] copper single-crystal specimens showed that dislocation configurations and twinning threshold using laser-induced shock waves (2.5 to 6 ns pulse duration) are very similar to those obtained at durations 10 to 100 times longer as in explosively driven flyer plate studies. Laser shock experiments present a unique characteristic: the rapid decay of the pulse enables a rapid quench of the region subjected to the high amplitude shock. The early experiments by Johari and Thomas[7] and more recent results by Murr,[8] Grace,[9] and Gray[10] showed cell sizes that decreased with increasing shock pressures. The laser-shock results by Meyers *et al.*[5,6] confirm these experiments.[7–10] These results are a clear confirmation that defects are generated at the shock front, corroborating the theoretical treatments of Smith,[1] Hornbogen,[11] Meyers,[12] Weertman,[13] and Mogilevskii.[14]

As a corollary to the investigation on shock-deformed [001] copper monocrystals,[5,6] it was decided to establish the effects of crystallographic orientation and pressure decay effects on the deformation microstructure. An early investigation by DeAngelis and Cohen[15] using flyer plate experiments showed that the threshold pressure for twinning was 14 GPa for [001] and 16 GPa for [111].

An important goal of the research whose results are presented herein is to provide a mechanistic, quantitative explanation. The focus of this article is also to study the effect of orientation and pressure decay at pressures ranging from

20 to 60 GPa. The specimens were shocked using a short-pulsed laser (2.5 to 10 ns initial pulse duration) and then recovered for analysis by TEM. The orientations considered in this analysis were [001] and [$\bar{1}$34], which is 14 deg off of [011], as shown in Figure 1. The [001] is a highly symmetric orientation with all four activated slip systems having identical Schmid factors. Unlike [001], the [$\bar{1}$34] orientation has much lower symmetry and therefore only one of the 12 available slip systems is preferentially activated. This article briefly discusses the experimental procedures used to carry out this study and microstructural analysis of recovered specimens. Correlation of the experimental results to a constitutive description of shock-compressed copper is carried out and confirms the orientation dependence of the threshold twinning pressure.

II. EXPERIMENTAL METHODS

High intensity, pulsed lasers are an excellent way to study shock compression effects in solids because pressures on the order of a 100 GPa and strain rates above 10^7 s^{-1} are possible due to the production of high energy densities and short pulses. Three different techniques were applied during these laser shock compression experiments in order to obtain a more complete understanding of shock-wave propagation through a crystalline material and the resulting material defects: *in-situ* dynamic X-ray diffraction, VISAR wave profile measurements, and recovery experiments for defect analysis. The results from the X-ray diffraction experiments and VISAR measurements are described elsewhere.[16]

For the recovery experiments, copper (99.999 pct pure) single crystals with orientations [001] and [$\bar{1}$34] were selected. The [001] orientation is highly symmetric, whereas [$\bar{1}$34] is asymmetric. The crystals with [001] orientation were obtained from Goodfellow, Inc. (Berwyn, PA) in the form of disks with diameters between 2 and 3 mm and a 1-mm thickness. Single-crystal samples with a [$\bar{1}$34] orientation were cut from a large bicrystal by electrodischarge machining (EDM) into cylinders with a 3-mm diameter and 5-mm length. They were mounted by press fitting into foam-filled recovery tubes shown in Figure 2. Foam with a density of 50 mg/cm^3 was used to decelerate the samples for recovery.

The shock experiments were primarily carried out at the OMEGA Laser Facility at the University of Rochester's Laboratory for Laser Energetics (Rochester, NY). Preliminary and follow-up experiments were performed using the JANUS Laser at the Lawrence Livermore National Laboratory (LLNL). The input laser energies used in the experiments were 70, 200, and 300 J for both [001] and [$\bar{1}$34]. The laser spot size was on the order of 2.5 to 3.0 mm depending on the diameter of the sample. The pulse duration was typically 2.5 ns with a small number of experiments occurring at 6 ns. The corresponding energy densities vary from 10 to 70 MJ/m^2. The energies can be translated into pressures using Lindl's equation:[17]

$$P = 4 \times 10^3 \left(\frac{I_{15}}{\lambda} \right)^{2/3} \quad [1]$$

where P is pressure (GPa), I_{15} is laser intensity (in 10^{15} W/cm^2), and λ is wavelength in micrometers. For example, for a laser pulse of 50 J with a pulse duration of 3 ns, a spot size of 0.001 m (1 mm), and the wavelength of the laser equal to 532 nm, one obtains an initial pressure of 100 GPa. In these experiments, 70 J is equivalent to 20 GPa, 200 J is equivalent to 40 GPa, and 300 J is equivalent to 60 GPa. In the following discussion, these initial values of pressures in GPa will be used to differentiate between the experiments.

Each of the 1-mm-thick [001] shocked specimens was sliced into two 0.5-mm discs (labeled A and B, respectively) using a slow-speed diamond saw or wire EDM and then mechanically ground to a thickness of 100 μm. The samples are approximately 0.25 and 0.75 mm from the laser-irradiated surface. The [$\bar{1}$34] cylinders with a length of 5 mm were sectioned for TEM examination according to Figure 3 by wire EDM and then also mechanically ground to a thickness of 100 μm. The [$\bar{1}$34] specimens (labeled A through E, respectively) after polishing are at approximately 0.25, 0.75, 1.25, 1.75, and 2.25 mm from the energy-depositing surface, as shown in Figure 3. The remaining 2.5 mm of the specimen was not used because of the rapid decay of the shock wave and the tension pulse from the reflected wave, which modifies the microstructure. The primary function of this region was to trap the reflected ten-

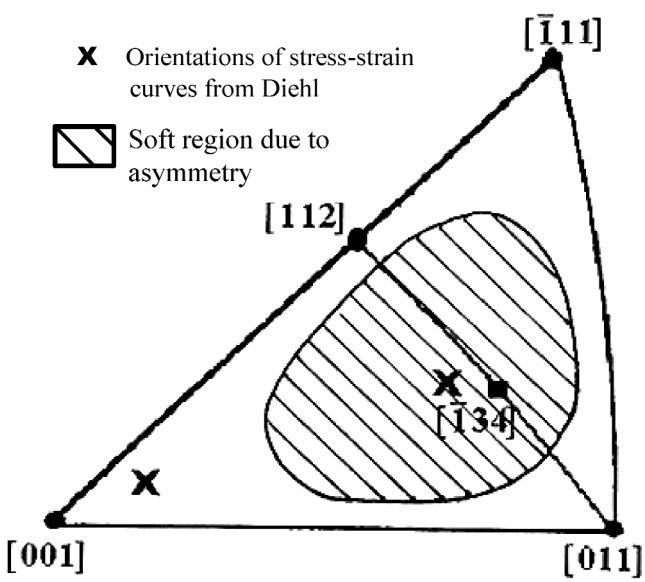

Fig. 1—Standard stereographic projection showing [001] and [$\bar{1}$34] orientations, which were used in the laser-shock experiments. The asymmetric orientation [$\bar{1}$34] is 14 deg from [011] and 38 deg from [001].

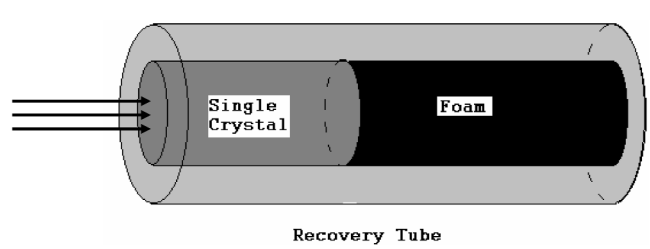

Fig. 2—Experimental setup for recovery of laser-induced shock compression of [001] and [$\bar{1}$34] copper specimens, recovery holder, and foam with a density of 50 mg/cm^3 to decelerate the shocked specimens.

sile waves. Thin foils were prepared for TEM examination by using a twin-jet Struers (Denmark) Tenupol-3 polisher with an electro-polishing solution composed by 7 vol. pct sulfuric acid in methanol at a temperature of −40 °C. The TEM observation was conducted in a PHILIPS* CM-30 microscope operating at 300 kV or a JEOL** 200CX operating at 200 kV.

*PHILIPS is a trademark of Philips Electronic Instruments Corp., Mahwah, NJ.

**JEOL is a trademark of Japan Electron Optics Ltd., Tokyo.

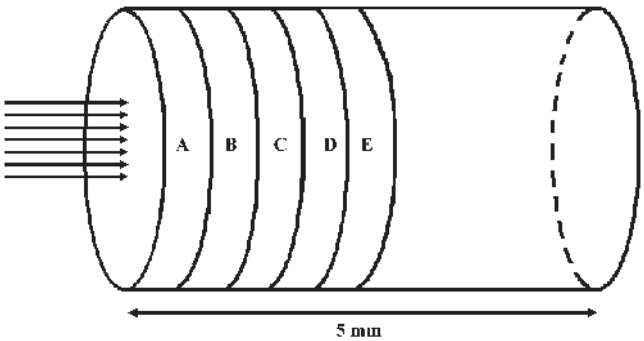

Fig. 3—Schematic of the [$\bar{1}$34] recovered specimen. Five thin foils for TEM observation were cut from each sample at a specific distance from the impact surface: A at 0.25 mm, B at 0.75 mm, C at 1.25 mm, D at 1.75 mm, and E at 2.25 mm.

The results of six shock recovery conditions are reported herein. The results obtained from [001] have been extensively discussed in Meyers *et al.*[5,6] and will only be described briefly in order to compare the results of the differing orientations. Since thin foils were prepared from samples cut at standard distances from the energy deposition surface, the direct observation of the change in residual microstructure with pulse decay could be made. The pressures can be predicted from computational simulations, as shown in Figure 4. The shock amplitude at the surface of the Cu crystal can be extracted from the incident laser energies and computed values using hydrocode calculations, calibrated against VISAR measurements. Results of the calculated pressure wave in [001] copper are shown in Figure 4 at varying pressures. Due

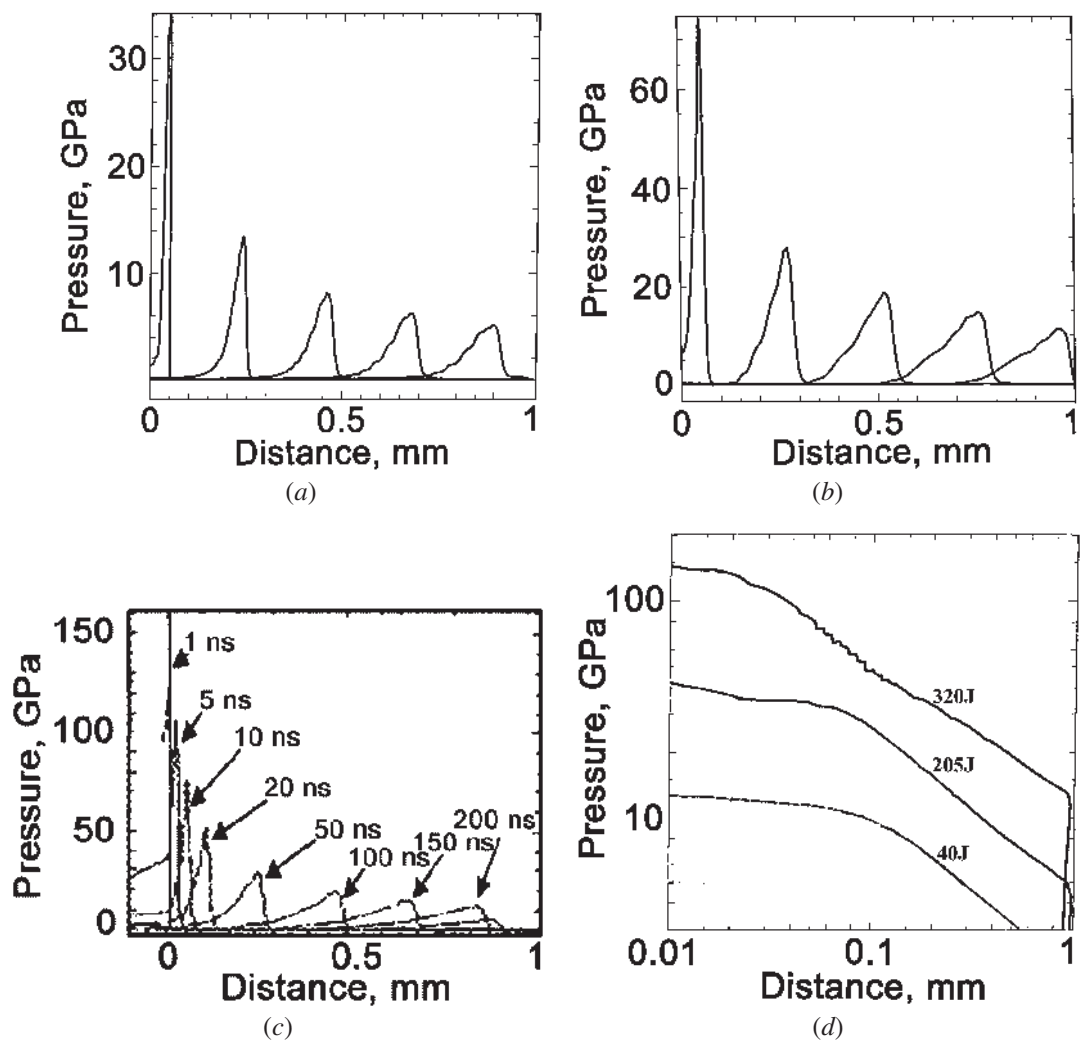

Fig. 4—Simulated pressure profiles as a function of distance from the energy deposition surface for three different incident laser energies: (*a*) 70 J, (*b*) 200 J, and (*c*) 300 J. (*d*) Maximum pressure as a function of distance from the illuminated surface for the three cases shown in (a) through (c). For each condition, the shock wave exponentially decreases in amplitude with distance traveled.

to the short duration of the shock created by the 3-ns laser pulse, the decay in the specimen is very rapid, as shown by the plotted pressure profiles. Snapshots of the pressure profiles in the Cu at times from 1 to 200 ns and up to a depth of 1 mm are shown in Figures 4(a), (b), and (c) for three initial energy levels: 70, 200, and 300 J. The amplitude of the pressure wave in the sample decays substantially and the pulse duration broadens as a function of distance. Figure 4(d) shows the decay of the maximum pressure in the specimens at these three energy levels. It can be seen that there is an exponential decrease as a function of propagation distance. This is a result of the release at the front free surface immediately following the end of the laser pulse.

Cell size measurements were carried out using TEM and applying a standard statistical approach. The dislocation density was obtained by a simple intercept method and is somewhat dependent on specimen thickness and, therefore, it is somewhat subjective. However, in thinner specimens, the cells invariably relax and a lower bound can be obtained. In thicker specimens (up to 1 μm), the measurement is difficult because the electron beam may transverse several cells, skewing the density measurements.

III. EXPERIMENTAL RESULTS

Copper has been the object of numerous shock recovery experiments and its response is fairly well understood at strain rates below 10^6 s^{-1}. It has a relatively high stacking-fault energy of 57 $\pm$ 8 mJ/m^2, which is similar to nickel, but only 2/3 of aluminum. Because of this high stacking fault energy, twinning is inherently difficult to obtain in copper, requiring either low temperatures or high strain rates. In shock-compressed copper, the defect substructure consists of dislocation cells up to a critical pressure. When higher pressures are obtained, twinning becomes not only possible, but the dominant deformation mechanism. For single crystals, De Angelis and Cohen[15] found that the crystal twinning pressure was 14 GPa for a shock wave propagating along [100], whereas it was 16 GPa for [111]. This is consistent with the findings by Nolder and Thomas[18,19] for nickel. Murr[8] and Grace[9] observed a cellular structure with the cell size decreasing from 0.7 μm at 5.5 GPa to 0.15 μm at 34.5 GPa. In this current effort, both orientation and pressure decay effects are examined with respect to the ensuing deformation microstructure.

Systematic differences are observed in the deformation substructures for the two crystal orientations and different laser-shock energy inputs. However, for a given input energy, in some shocked specimens, changes in deformation substructure in the electron transparent regions surrounding the thin foil perforation were observed. This is consistent with the area illuminated by the laser beam, which is on the order of the copper specimen area. It is also consistent with the fact that the laser energy is not spatially uniform, being highest at the center. The laser experiments use phase plates to minimize this effect, which causes the energy to be spread more evenly over the surface. There exists some slight variation, but this is expected to disappear as the shock wave progresses through the sample. For a nominal hole made by electropolishing of about 200 μm, the regions examined can be up to 250 μm apart, as measured. With this in mind, specific steps were taken to document the entire deformation substructure around the entire region: This would be indicative of substructure variations implicit in such laser-shocked tests. It was found, however, that the residual defect substructure was typically uniform.

The unshocked copper crystal shows only a limited number of dislocations without preferred alignments or arrangements. The dislocation density is typically that of an undeformed crystal (on the order of 10^{11}-10^{12} m^{-2}).

A. *Deformation Microstructure of Specimens Shocked at 20 GPa (70 J)*

The [001] orientation shocked at 20 GPa contains a well-defined cellular organization of 1/2<110> dislocations with average cell size diameters between 0.2 and 0.3 μm (Figure 5(a)). The microstructure was homogeneous through-

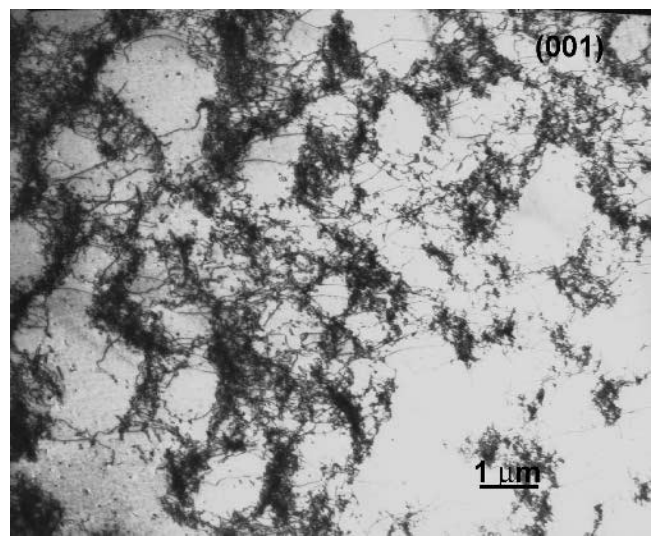

(*a*)

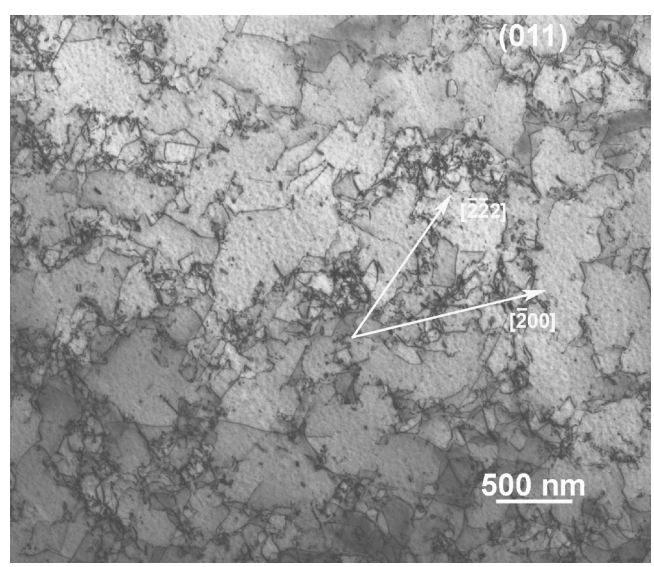

(*b*)

Fig. 5—TEM images of the defect substructures of monocrystalline copper shocked with laser energies of 70 J: (*a*) [001] orientation is comprised of dislocation cells, TEM beam direction, B = [001], diffraction vector, g = [020]; and (*b*) dislocation cells in orientation [$\bar{1}$34], beam direction B = [011], g = [2$\bar{2}$2].

out the sample. Qualitatively, these results confirm previous observations, albeit at a pulse duration that is lower by a factor of 10 to 100 than that applied by Murr.[7] The predicted cell size from Murr's data,[7] at a pressure of 12 GPa, is 0.4 μm, and for 20 GPa, it is 0.25 μm. The observed cell size is also consistent with Gray's[10] measurements: 0.5 μm/10 GPa. However, the dislocation density ($\sim 10^{13}$ to 10^{14} m^{-2}) and related cell-wall thickness seem to be lower than in these previous studies, which may be a result of the higher strain rates and shorter relaxation times.

The [$\bar{1}$34] orientation shocked at 20 GPa contains a similar well-defined cellular network comprised of 1/2<110> dislocations with a slightly larger (0.3 to 0.4 μm) average cell size (Figure 5(b)). The dislocation density is on the order of 10^{13} m^{-2}. The cells are comprised primarily of three dislocation systems: (111)[$\bar{1}$01], (111)[1$\bar{1}$0], and ($\bar{1}$11)[101], as indicated in Table I. Figures 6(a) through (d) is a systematic analysis of the [$\bar{1}$34] dislocation systems and the given dislocations are marked in the figures as primary (P), secondary I (S_I), and secondary II (S_{II}). In Figure 6(a), all three slip systems are shown with a $g = (\bar{2}00)$; Figure 6(b) shows the two secondary slip systems as visible and the primary system as invisible with $g = (\bar{1}1\bar{1})$; Figure 6(c) shows the primary slip system as visible and the two secondary slip systems as invisible, $B = [011]$, $g = [11\bar{1}]$; and Figure 6(d) shows the primary slip system and secondary slip system (111)[1$\bar{1}$0] as visible and the secondary slip system ($\bar{1}$11)[101] as invisible.

Table I. Resolved Shear Stress on the Activated Slip Systems in [001] and [$\bar{1}$34] for Copper Monocrystals

Shock Direction	Slip Plane (n)	Slip Direction (s)	Schmid Factor (M)	τ_{RSS} at 40 GPa	τ_{RSS} at 60 GPa
[001]	(111)	[0$\bar{1}$1] and [$\bar{1}$01]	0.4082	16.4	24.5
	($\bar{1}$11)	[0$\bar{1}$1] and [101]	0.4082	16.4	24.5
	(1$\bar{1}$1)	[011] and [$\bar{1}$01]	0.4082	16.4	24.5
	(11$\bar{1}$)	[0$\bar{1}\bar{1}$] and [101]	0.4082	16.4	24.5
[$\bar{1}$34]	(111)	[$\bar{1}$01]	0.4711	18.8	28.3
	(111)	[1$\bar{1}$0]	0.3768	15.1	22.6
	($\bar{1}$11)	[101]	0.3768	15.1	22.6
	($\bar{1}$11)	[110]	0.2512	10.0	15.1
	(11$\bar{1}$)	[0$\bar{1}\bar{1}$]	0.2198	8.8	13.2
	($\bar{1}$11)	[0$\bar{1}$1]	0.1256	5.0	7.5

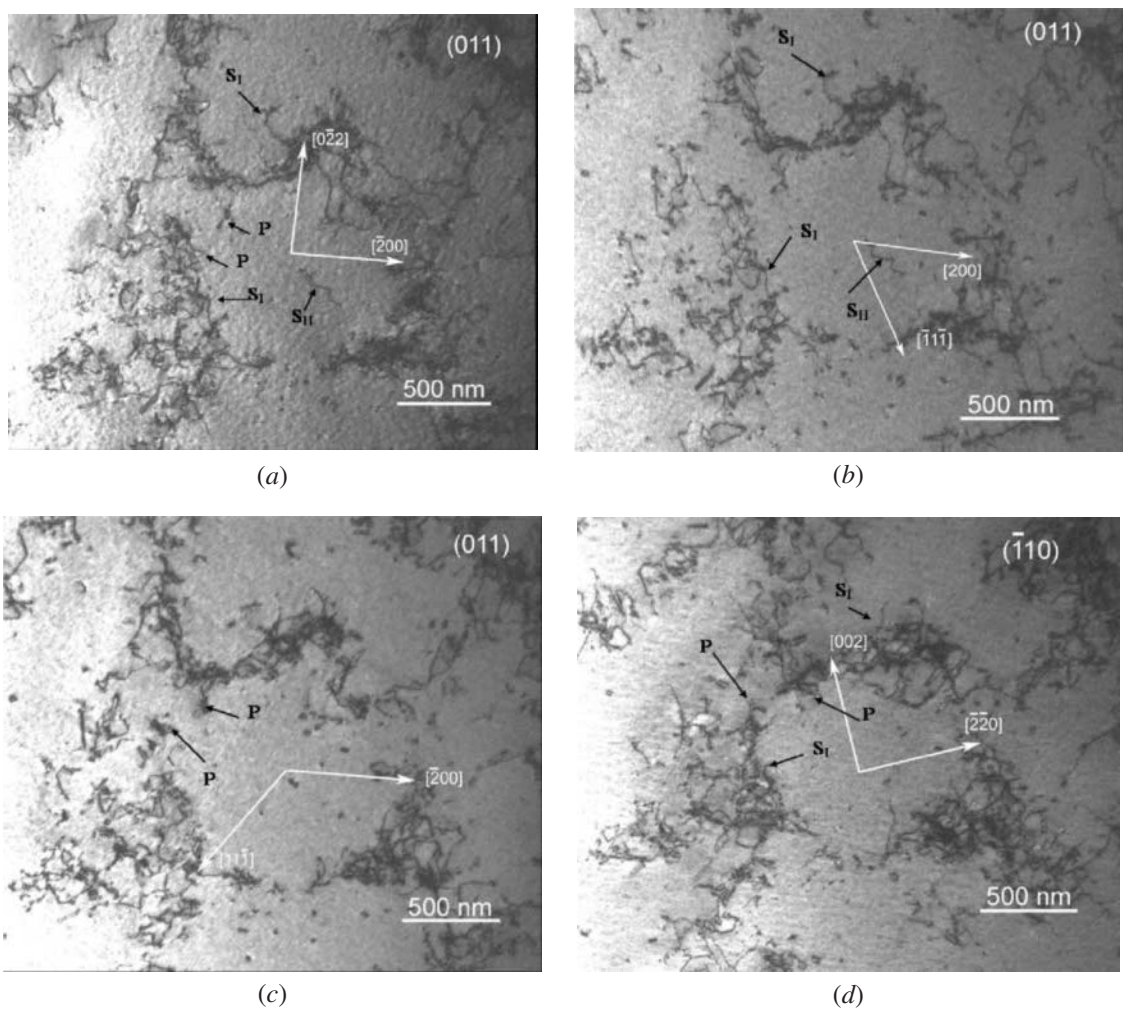

Fig. 6—Dislocation analysis of monocrystalline copper oriented to [$\bar{1}$34] shocked with laser energies of 70 J: (*a*) three dominating slip systems are visible, $B = [011]$, $g = [\bar{2}00]$; (*b*) primary slip system [111]($\bar{1}$01) is invisible, $B = [011]$, $g = [\bar{1}1\bar{1}]$; (*c*) two secondary slip systems (111)[1$\bar{1}$0] and ($\bar{1}$11)[101] are invisible, $B = [011]$, $g = [11\bar{1}]$; (*d*) secondary slip system ($\bar{1}$11)[101] is invisible, $B = [\bar{1}10]$, $g = [002]$.

Note that (111)[$\bar{1}$01] is the primary slip system, which is activated in conjunction with the coplanar (111)[1$\bar{1}$0] and the conjugate ($\bar{1}$11)[101] slip systems. Several other slip systems are also activated since the resolved shear stress exceeds the critical value for most of the potential systems. However, it was observed that the contribution to the dislocation density from these other slip systems is relatively small compared to the dislocations associated with the primary and secondary slip systems with much higher Schmid factors.

B. *Deformation Microstructure of Specimens Shocked at 40 GPa (200 J)*

For the [001] orientation, this intermediate energy input creates dense dislocation tangles, stacking faults, and microtwins. Figure 7(a) shows stacking faults and dislocation tangles marked as DT and SF. There are no readily discernible dislocation cells. Furthermore, the observed deformation substructure appears uniform around the thin foil perforation. These features are significantly different than the deforation substructure observed at the lower laser energy (Figure 5(a)) in what can be construed as a pressure-dependent change in the deformation mechanism. Perpendicular traces of planar features are seen when the beam direction is <001>. These correspond to traces of {111} on (001). All four stacking fault variants, *viz*, the partial dislocations (11$\bar{1}$)1/6[112], (111)1/6[$\bar{1}\bar{1}$2], ($\bar{1}$11)1/6[1$\bar{1}$2], and (1$\bar{1}$1)1/6[$\bar{1}$12], are observed. Given the incident energy input is parallel to [001], it is not surprising that all four stacking fault variants are activated (Figure 7(a)), because they all have the same Schmid factor (Table I).

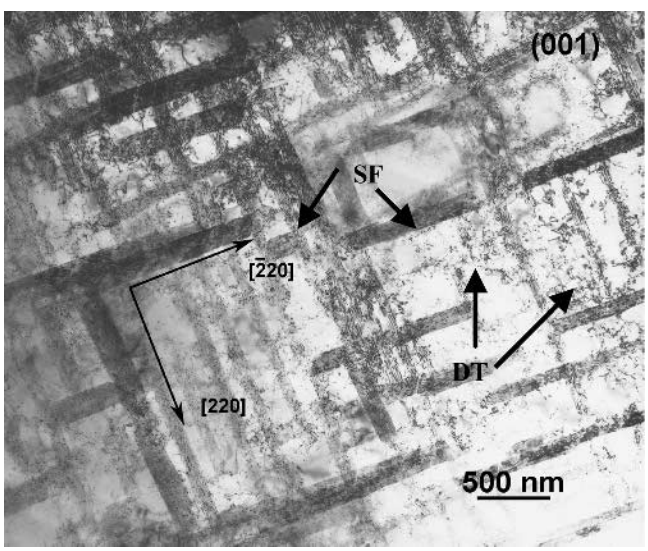

(*a*)

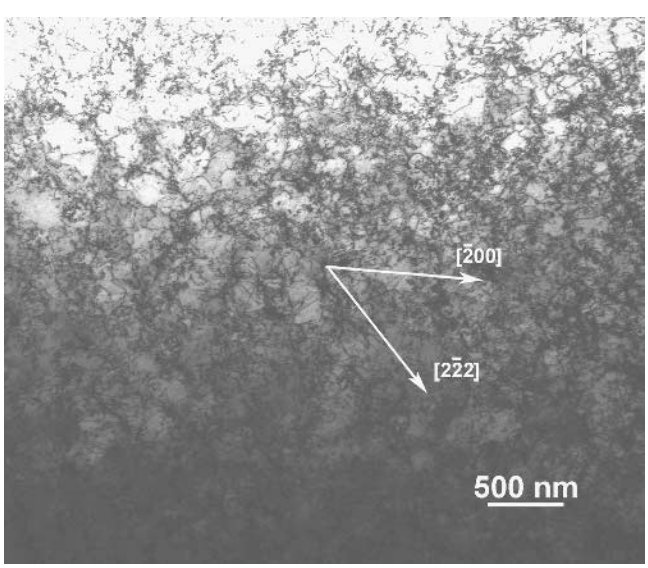

(*b*)

Fig. 7—Defect substructures of monocrystalline copper shocked with laser energies of 200 J: (*a*) [001] showing four variants of stacking faults, B = [001], g = [$\bar{2}$20]; and (*b*) [$\bar{1}$34] showing a dense network of dislocation cells on the order of 150 nm.

For the [$\bar{1}$34] orientation, the deformation substructure continues to be cellular, albeit finer at a 0.15-μm average cell size and a significantly higher dislocation density (10^{14} m^{-2}, Figure 7(b)). This is in direct contrast to the mechanism change observed in [001]. Again, the three slip systems previously described dominate the deformation substructure. A large number of loops are also visible. These were found to contribute to the cell walls and were commonly observed within the cells in a very low concentration.

C. *Deformation Microstructure of Specimens Shocked at 60 GPa (300 J)*

The deformation microstructure of the [001] orientation shocked at 60 GPa consists of a high density of microtwins and laths (Figures 8(a) and (b)). The deformation is not uniform around the perforation, with the microtwins situated closer to the center of the sample and the laths away from the center. Two sets of microtwins are observed in the thin foils (not shown here). When imaged at B = [001], they appear at exactly 90 deg to each other aligned along [220] and $\bar{2}$20] directions; they are present roughly in the same proportion. When imaged in the edge orientation at B close to [$\bar{1}$01] (Figure 8(a)), the microtwins from the first set have a (111) habit plane and are elongated along [1$\bar{2}$1]. This set of microtwins exhibits a wide range of lengths, from as small as 70 nm to as large as 1 μm; the mean value is around 125 nm. In contrast, the second set of micro-twins has a near uniform length of 70 nm.

Unlike the microtwins, the laths are elongated close to <220>. In some regions, they are aligned along [$\bar{2}$20], and in others, along [220]. The intermediate area shows laths misoriented from [220]. Given the curvature of the laths, it is unlikely that they conform to any single habit plane. Nonetheless, the projected width of the lath interface shows a minimum at B = [001], and a maximum at either [101] or [$\bar{1}$01] where the respective {111} are in the edge orientation. The interfacial between laths is parallel to [001] and therefore uniquely different from microtwins. In fact, on rare occasions, we observe laths containing some microtwins (Figure 8(b)). These features are in total agreement with the "wavy subgrains" observed after high-pressure shock compression by Murr[8] (in particular, note similarities with Figures 34 and 35 of Reference 8). This structure is also analogous to the one observed by Gray[10] in specimens where the residual strain was high. Thus, it is suggested that the substructures revealed by Figures 8(a) and 8(b) are due to thermal recovery of the shock-induced microstructure. The orientation close

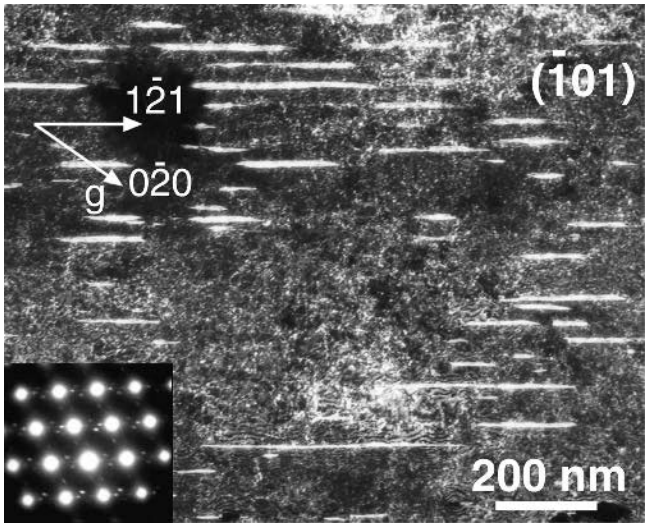

(*a*)

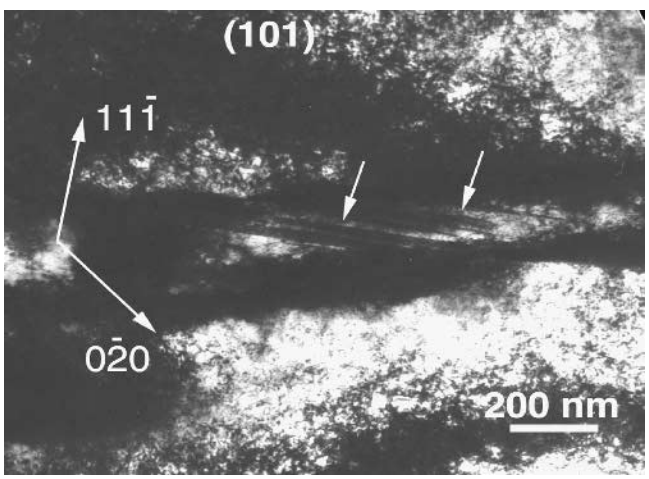

(*b*)

Fig. 8—Defect substructures of monocrystalline copper oriented to [001] shocked with laser energies of 300 J: (*a*) large density of microtwins, $B = [\bar{1}01]$, $g = [0\bar{2}0]$; and (*b*) microtwins contained within wavy grain lath features, $B = [101]$, $g = [020]$.

to {111} of the boundaries is a residue of the original twin boundaries. This microstructure represents the recovered state of a heavily twinned and dislocated structure.

For the $[\bar{1}34]$ orientation, the deformation substructure continues to be dominated by a dense cellular network of dislocations with regions of microtwins. Under these conditions, it is difficult to define the cell sizes except to say that the cell size is below 100 nm. These results are consistent throughout the thin areas examined. A number of microtwins are observed within the sample with lengths ranging from 50 nm to 1 μm and an average between 200 and 300 nm and widths of 20 to 30 nm. These occur on the twinning system with the highest Schmid factor, $[\bar{2}11]$ (111), as listed in Table II. Images of the twin-dominated and slip-dominated regions are shown in Figures 9(a) and (b), respectively.

It was found that the [001] deformation substructure evolution is systematic. As pressure increases, dislocation density increases and average cell size decreases until a critical density occurs and stacking faults form. At higher pressures,

Table II. Resolved Shear Stress on the Activated Twinning Systems in [001] and $[\bar{1}34]$ for Copper Monocrystals

Shock Direction	Twin Plane (n)	Twin Direction (s)	Schmid Factor (M)	τ_{RSS} at 40 GPa	τ_{RSS} at 60 GPa
[001]	$(\bar{1}11)$	$[1\bar{1}2]$	0.4714	18.8	28.2
	$(1\bar{1}1)$	$[\bar{1}12]$	0.4714	18.8	28.2
	(111)	$[11\bar{2}]$	0.4714	18.8	28.2
	$(11\bar{1})$	$[\bar{1}\bar{1}2]$	0.4714	18.8	28.2
$[\bar{1}34]$	(111)	$[\bar{2}11]$	0.4895	19.6	29.4
	$(1\bar{1}1)$	$[\bar{1}\bar{1}\bar{2}]$	0.3857	15.4	23.1
	$(1\bar{1}1)$	$[1\bar{1}\bar{2}]$	0.3857	15.4	23.1
	$(\bar{1}11)$	[211]	0.3626	14.5	21.7
	$(11\bar{1})$	$[\bar{1}21]$	0.1714	6.9	10.3

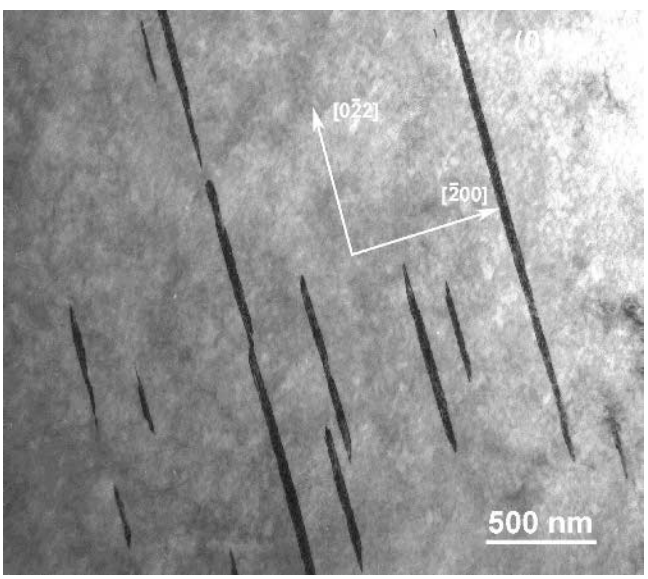

(*a*)

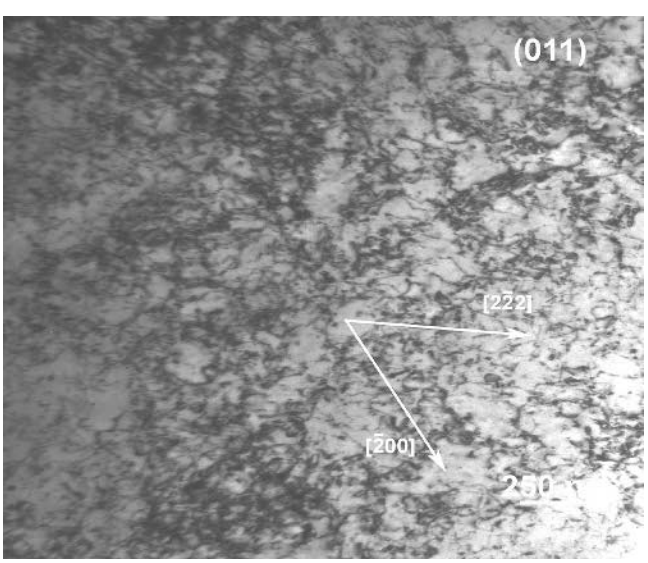

(*b*)

Fig. 9—Defect substructures of monocrystalline copper oriented to $[\bar{1}34]$ shocked with laser energies of 300 J: (*a*) region with a high density of twinning, $B = [011]$, $g = [\bar{2}00]$; and (*b*) region of dense dislocation cells, $B = [011]$, $g = [2\bar{2}2]$.

twins are widely observed. The evolution of the substructure in [$\bar{1}$34] is substantially different. At lower pressures, changes in dislocation densities and cell sizes are similar; however, twinning is found only sporadically at the highest pressure of 60 GPa. Stacking faults are also a rare occurrence in the [$\bar{1}$34] orientation.

D. *Pressure Decay Effects: [$\bar{1}$34] Orientation*

Figures 10(a) through (d) show the dislocation cells for the 20 GPa (70 J) at four locations: A, B, D, and E. The decay in pressure, shown in Figure 4(a), is accompanied as expected by an increase in cell size and decrease in dislocation density. The average cell size varies from 0.40 μm for A (Figure 10(a)) growing to 0.85 μm in B (Figure 10(b)), 1.6 μm in D (Figure 10(c)), and to 3 μm in E (Figure 10(d)). The number of activated slip systems is reduced as expected because the shear stress from the pressure wave decays. This, in part, leads to a decrease in cell wall thickness and a decrease in dislocation density from 10^{13} m^{-2} for the front surface to densities on the order of 10^{10} m^{-2} for the back surface.

For the 40 GPa (200 J) experiments, cell sizes and dislocation densities follow the same patterns, as shown in Figures 11(a) through (e). Figure 4(b) shows the calculated pressure decay. The tightly packed cell sizes are obtained as expected from the higher pressures. The average cell sizes are 0.14 μm for specimen A, 0.22 μm for specimen B, 0.41 μm for specimen C, 0.76 μm for specimen D, and 1.43 μm for specimen E. The dislocation densities decrease from 10^{14} m^{-2} at the front to 10^{11} m^{-2} at position E.

The 60 GPa (300 J) level is marked by the onset of twinning. Figure 12(a) shows the dense tangles of dislocations and deformation twins on a near edge-on orientation for position A from the laser-irradiated surface. The average width of the

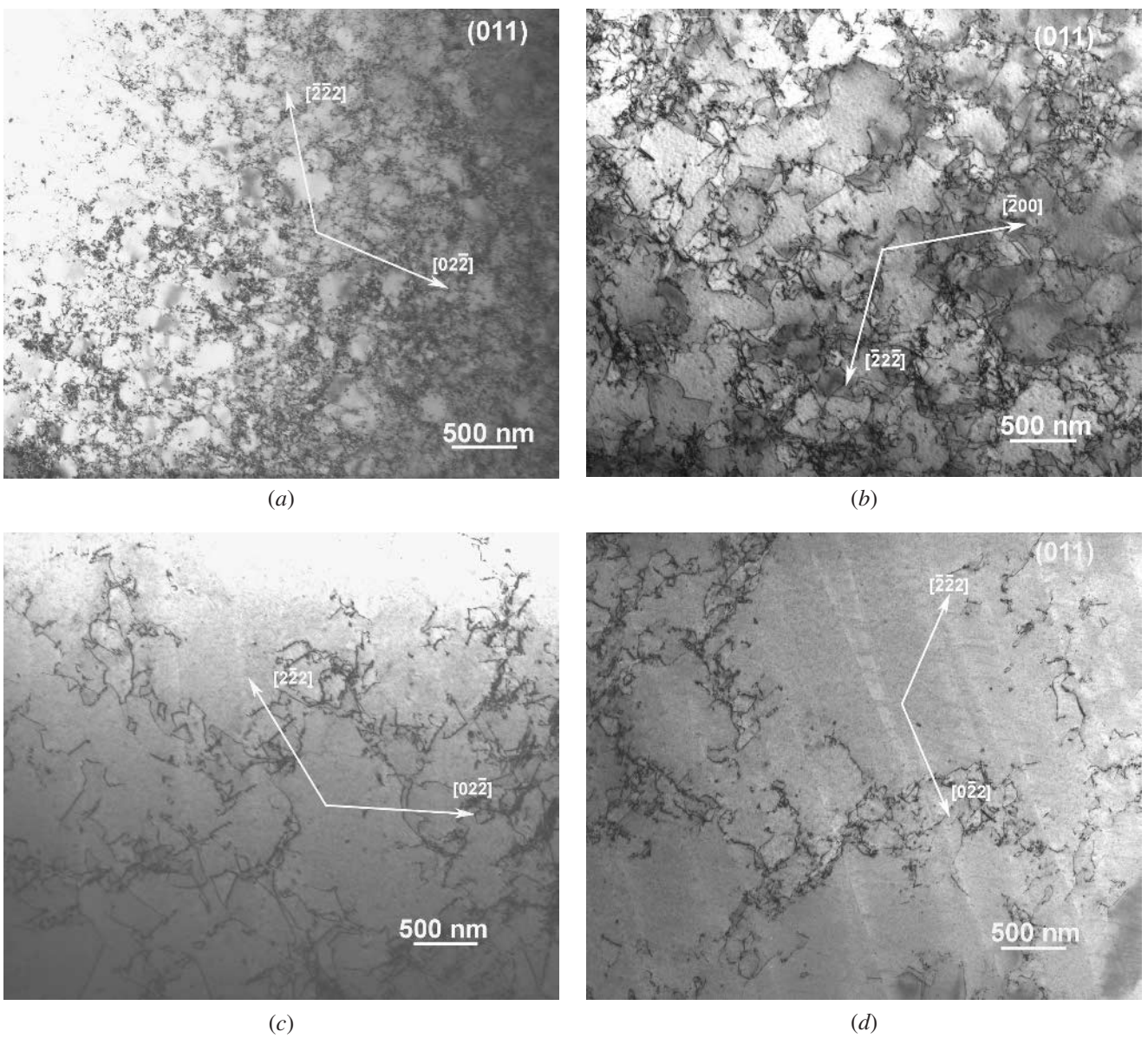

Fig. 10—TEM images of the defect substructures showing the pressure decay effects of [$\bar{1}$34] at different distances from the laser irradiated surface using laser energy at 70 J (B = [011] for each image): (*a*) 0.25 mm, g = [$\bar{2}$2$\bar{2}$]; (*b*) 0.75 mm, g = [$\bar{2}\bar{2}$2]; (*c*) 1.75 mm, g = [2$\bar{2}$2]; and (*d*) 2.25 mm, g = [$\bar{2}\bar{2}$2].

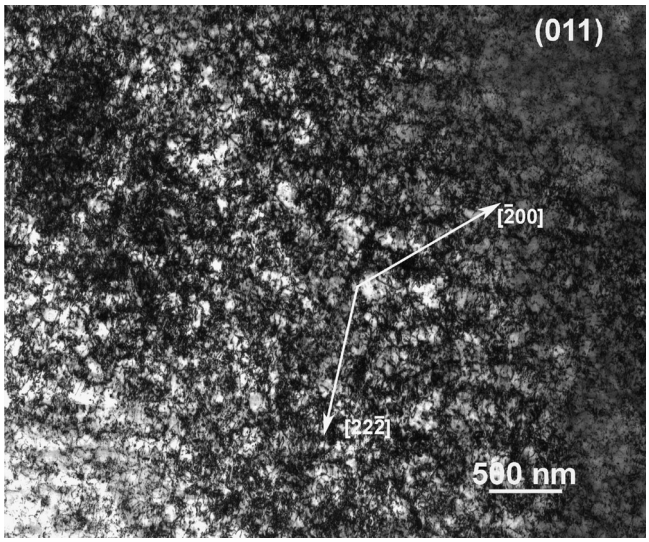

(*a*)

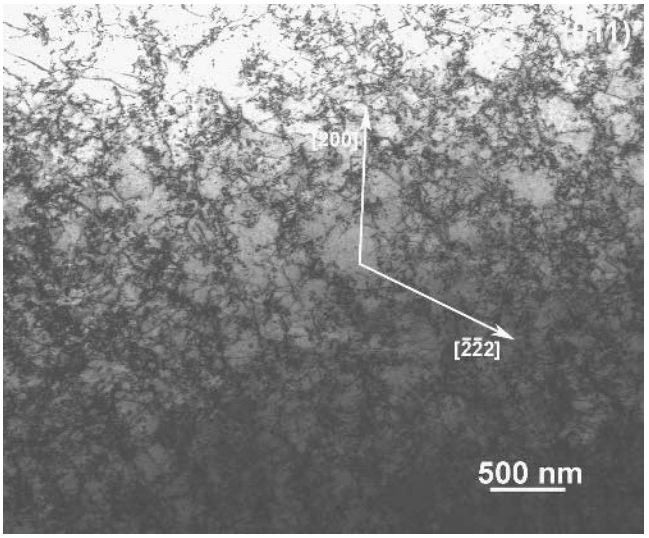

(*b*)

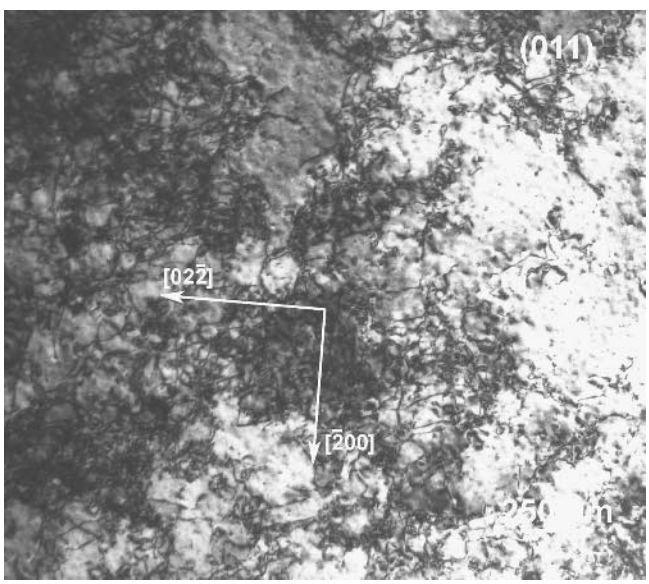

(*c*)

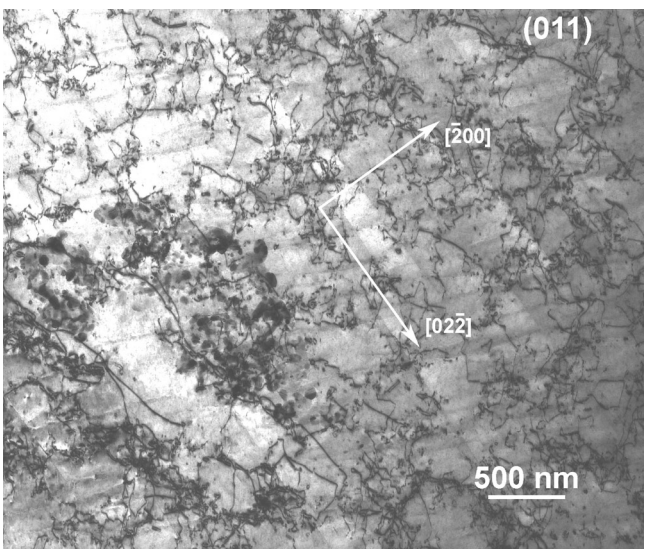

(*d*)

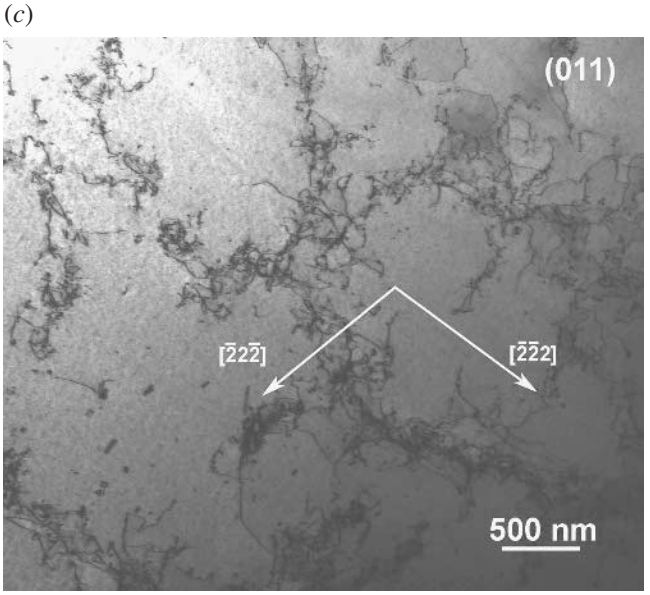

(*e*)

Fig. 11—TEM images of the defect substructures showing the pressure decay effects of [$\bar{1}$34] at different distances from the laser irradiated surface using 200 J of laser energy (for each image, B = [011]): (*a*) 0.25 mm, g = [22$\bar{2}$]; (*b*) 0.75 mm, g = [$\bar{2}\bar{2}$2]; (*c*) 1.25 mm, g = [02$\bar{2}$]; (*d*) 1.75 mm, g = [02$\bar{2}$]; and (*e*) 2.25 mm, g = [$\bar{2}$2$\bar{2}$].

twins is nearly 50 nm and their length ranges from 0.5 to 2.5 μm. At B, the surface (Figures 12(b) through (d)), no deformation twinning was observed and the cell size ranged from 0.1 to 0.2 μm, which increased further to 0.20 to 0.25 μm at C and 0.4 to 0.5 μm at D, which is furthest from the drive surface. The dislocation densities are near saturation (10^{15} m^{-2}) at the front surface decaying to 10^{12} to 10^{13} m^{-2} at D.

In Figure 13(a), the cell sizes as a function of distance from laser-irradiated surface are plotted for the three energies. The cell sizes vary consistently with the three energy levels. Figure 13(b) shows that the size and pressure correlate at different locations within the specimen.

E. *Characterization of Loops*

One interesting feature is the observation of a large number of loops. For example, loops as small as 25 nm and as large as 250 nm are indicated in Figure 14. Given the density of loops observed, far greater than that observed in undeformed Cu, it is reasonable to suggest that loop nucleation is an essential event of laser-induced shock compression and could provide a mechanism of dislocation nucleation in monocrystalline metals. Indeed, this has recently been reported by Meyers *et al.*[6] These loops are found both within the cell walls and within the cells. This is another interesting feature at this pressure as these dislocations appear to be pinned on particles or defects that are not discernible at the resolution available in the present TEM observations. While not specifically indicated in the micrographs, a large number of small (about 10 nm) dislocation loops were observed. The isolated pinned dislocations point to some pinning events similar to the case in samples deformed at lower pressures (20 GPa). The aim of future work is to characterize the nature of these loops and provide a mechanism

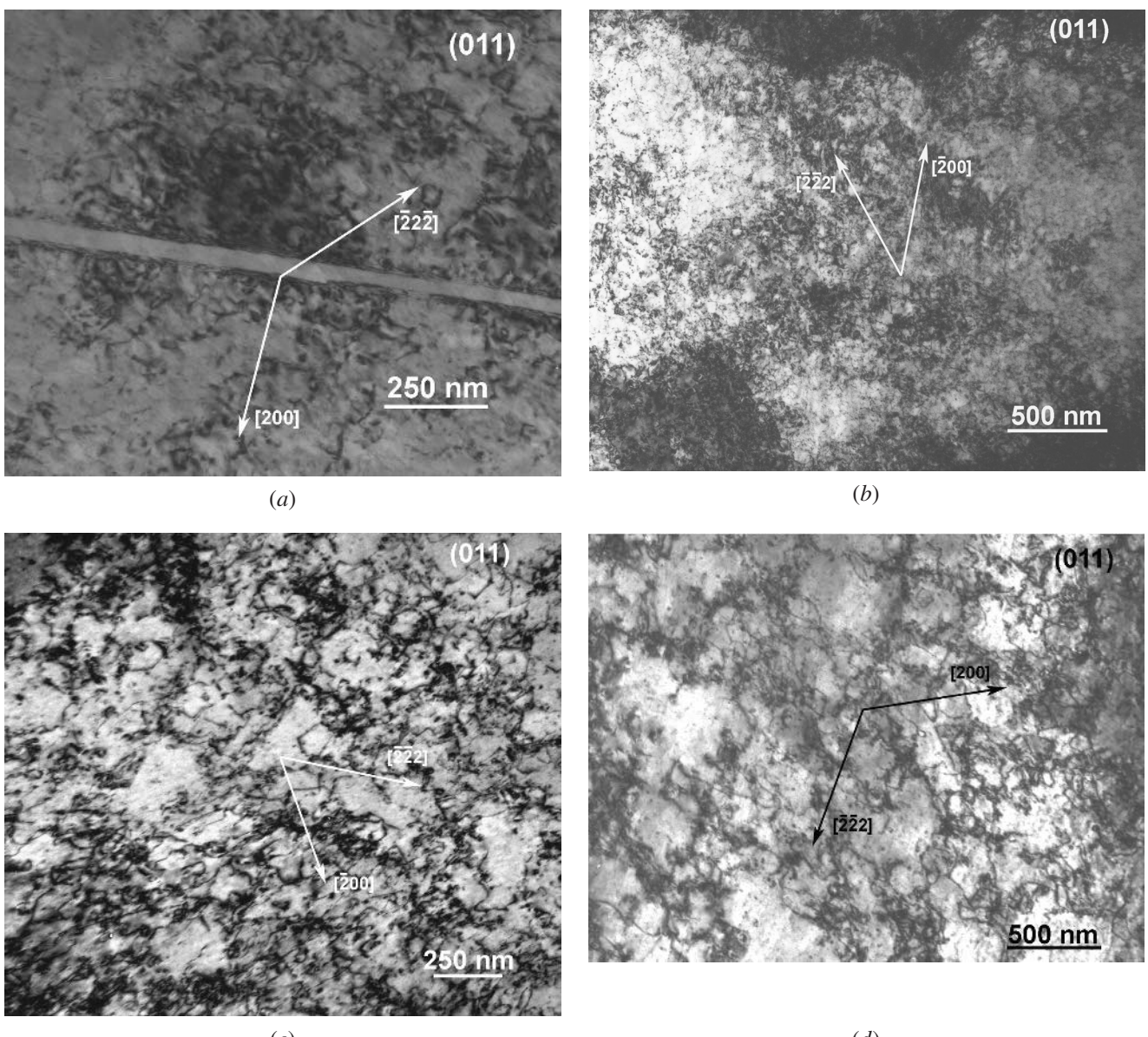

Fig. 12—TEM images of the defect substructures showing the pressure decay effects of [$\bar{1}$34] at different distances from the laser irradiated surface using 300 J of laser energy (for each image, B = [011]): (*a*) 0.25 mm, g = [200]; (*b*) 0.75 mm, g = [$\bar{2}\bar{2}$2]; (*c*) 1.25 mm, g = [$\bar{2}$00]; and (*d*) 1.75 mm, g = [$\bar{2}\bar{2}$2].

for their development at these time scales. Dipole interaction, pinning of dislocations, lattice relaxation of dislocations, and coalescence of vacancies caused by jog drag are all possible mechanisms. It is also possible that loops form through more than one mechanism since the loops have substantially different sizes and shapes. These loops could also be a source for void nucleation when the strength of the shock exceeds the spall strength of the material.

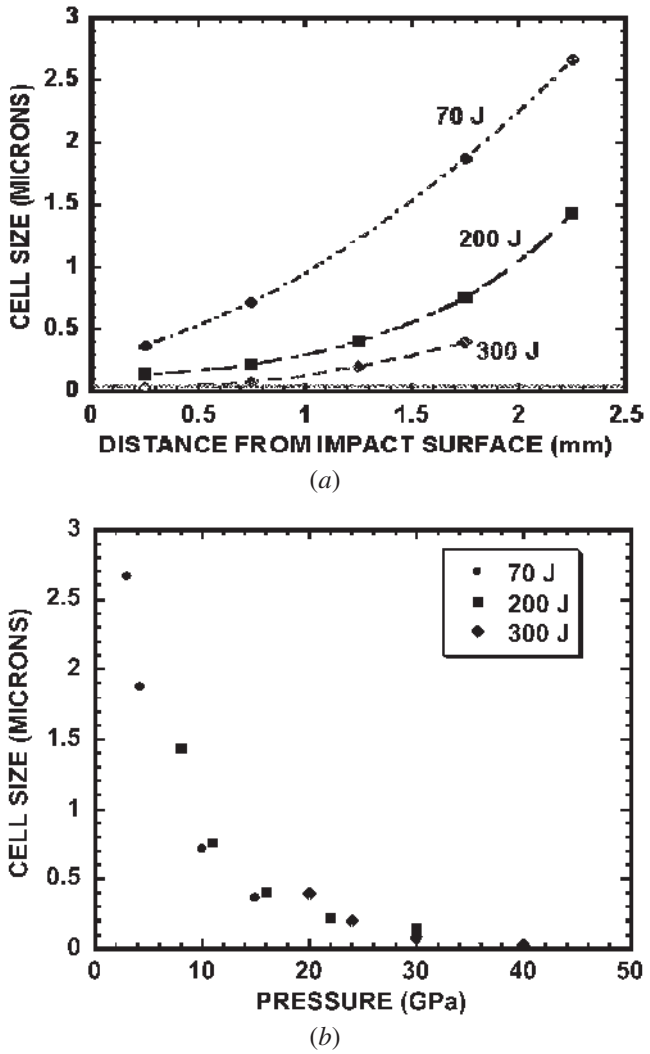

Fig. 13—(*a*) Cell size as a function of distance from the impact surface for the [$\bar{1}$34] crystal orientation at the three energies: 70, 200, and 300 J. Twinning is observed when dislocation cell sizes fall below an average size of 0.05 μm, as represented by the bottom line. (*b*) Cell size as a function of estimated pressure for the three energy levels.

IV. ANALYSIS

In this section, the microstructural development will be quantitatively analyzed. The [$\bar{1}$34] and [001] crystallographic orientations, marked in Figure 1, are representative of two contrasting regions. The central region of the stereographic projection is marked "soft" because this area corresponds to the single slip domain (the [$\bar{1}$34] is near its center). The corners of the stereographic triangle deform by multislip; [001] is typical. The corresponding stress-strain curves obtained by Diehl[20] are shown in Figure 15. Though the orientations are not exactly the same as the experiments (the relative positions are shown in Figure 1), the stress-strain curves are similar to the expected curves from the given orientations. The differences between the two curves [001] and [$\bar{1}$34] may appear moderate, but in fact, they are a result of substantially different deformation behavior. The [$\bar{1}$34] orientation has a sizable easy glide region, as noted in Figure 15, followed by linear hardening, whereas [001] is symmetric and several slip systems are activated simultaneously, resulting in immediate cross-slip and an increased rate of hardening.

The existence of a twinning threshold at high pressures and high strain rates in fcc metals is well documented, but the effect of orientation has never been quantified. Part of the difficulty is the less than adequate theoretical understanding that exists to explain the deformation mechanism transition. One of the major goals of the current research is to develop a better constitutive description of the monocrystals and to correlate the experimentally obtained twinning threshold stress with theoretical predictions. The methodology to be used in the prediction of the threshold shock amplitude was delineated by Murr *et al.*[21] and Meyers *et al.*[22] and will only be briefly reviewed here and then applied to the different conditions previously described.

It is known that different fcc metals have different threshold pressures for the initiation of twinning, and Murr[23] showed that this pressure is dependent upon the stacking-fault energy. Slip and twinning are competing mechanisms.[22]

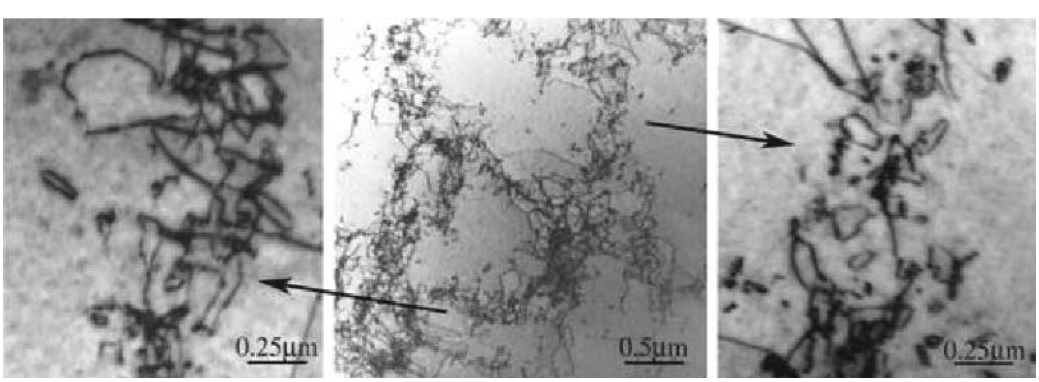

Fig. 14—Transmission electron micrograph of [$\bar{1}$34] shocked monocrystalline copper showing a large number of dislocation loops in the cell walls; right and left photographs are higher magnification of center photograph, B = [011].

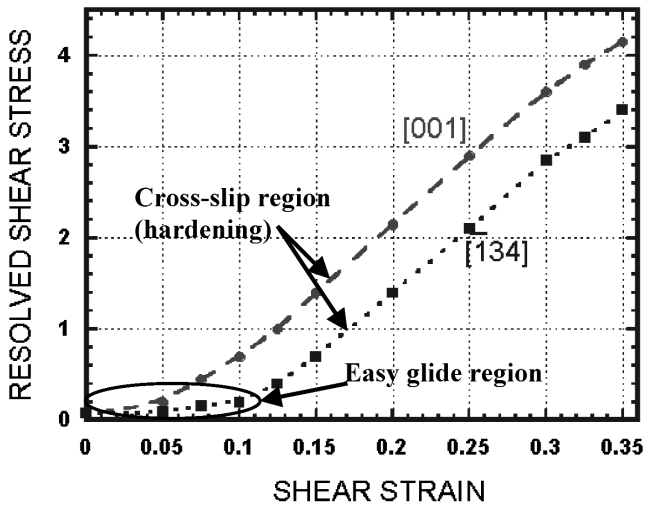

Fig. 15—Work-hardening curves obtained from Diehl[20] for the [001] and [$\bar{1}$34] orientations. The exact orientations are shown in Fig. 1. Because of the symmetrical nature of the [001] orientation, it has a smaller easy glide region than the [$\bar{1}$34] orientation.

Plastic deformation by slip has a strain rate and temperature dependence well described by the theory of thermally activated obstacles; it is reasonable to assume that slip is highly favored under most conditions. This assumption is corroborated by the experimental evidence presented in Section III.

The Schmid factors for slip and twinning for the two crystals are given in Tables I and II, respectively. It is clear that Schmid factors alone cannot account for the significant differences in the microstructure and threshold pressure for twinning. Since Schmid factors are simple one-dimensional calculations, system interactions and hydrostatic compression effects, which alter the deformation kinematics, are neglected. However, Schmid factors aid in the determination of the dominate slip and twinning systems for these two orientations.

The [001] has eight slip systems with identical Schmid factors. This is in accord with the microstructural observations of Section III (e.g., Figure 5(a)). For [$\bar{1}$34], [111] ($\bar{1}$01) is the primary slip system with a Schmid factor of 0.4711. Two slip systems, (111) [1$\bar{1}$0] and ($\bar{1}$11) [101], have slightly lower Schmid factors (0.3768). All three slip systems were observed. Figures 6(a) through (d) show a systematic TEM analysis confirming this.

The [001] crystal has four twinning systems belonging to {111} <112>. Each of these systems have identical Schmid factors (0.4714), as shown in Table II. The [$\bar{1}$34] crystal has one primary twinning system, [111] (1$\bar{1}\bar{2}$), and two secondary slip systems ($\bar{1}1\bar{1}$)[$\bar{1}$12] and ($\bar{1}1\bar{1}$)[11$\bar{2}$]. The corresponding Schmid factors for these three systems are, 0.4895, and 0.3857, respectively.

One can obtain the critical stress for the slip-twinning transition as a function of ε, $\dot{\varepsilon}$, and T. The application of this criterion to the shock front necessitates the knowledge of the strain rate. The strain rate at the shock front has been established by Swegle and Grady[24] to be, as a function of pressure, P:

$$P = k_{SG}\dot{\varepsilon}^{1/4} \qquad [2]$$

where k_{SG} is an empirical parameter.

Two separate aspects have to be considered in the analysis: (a) shock heating and (b) plastic strain at the shock front. Both shock heating and plastic strain by slip (and the associated work hardening) alter the flow stress of material by slip processes and need to be incorporated into the computation. The shock temperature, T_S, is a thermodynamic function of pressure (e.g., 25). It is obtained from the Rankine–Hugoniot equations and the Grüneisen equation of state. The internal energy of the shocked material is converted into temperature through the heat capacity and density:

$$T_S = T_0 \exp\left[\frac{\gamma_0}{V_0}(V_0 - V)\right] + \frac{(V_0 - V)}{2C_v}P + \frac{\exp[(-\gamma_0/V_0)V]}{2C_v} \int_{V_0}^{V} P \cdot \exp\left[(\gamma_0/V_0)V\right]\left[2 - \left(\frac{\gamma_0}{V_0}\right)(V_0 - V)\right]dV \qquad [3]$$

where V_0 and V are the initial and compressed specific volumes, respectively; γ_0 is the Grüneisen parameter for the material; and P and C_v are the pressure and heat capacity, respectively. The total (elastic + plastic) uniaxial strain, ε, at the shock front is related to the change in specific volume by

$$\frac{V}{V_0} = e^{\varepsilon} \qquad [4]$$

By inserting Eq. [4] into the P–V Hugoniot relationship, we obtains

$$P = \frac{C_0^2(1 - e^{\varepsilon})}{V_0[1 - S(1 - e^{\varepsilon})]^2} \qquad [5]$$

The constitutive response of the copper monocrystal is represented by the modified MTS expression:

$$\sigma_s = \sigma_0 f(\varepsilon)\left[1 - \left(\frac{kT}{G\mathbf{b}^3 g_0}\ln\left(\frac{\dot{\varepsilon}_0}{\dot{\varepsilon}}\right)\right)^{2/3}\right]^2 \qquad [6]$$

The thermal and strain-rate parameters p, q, g_0, and $\dot{\varepsilon}_0$ are taken from Follansbee and Gray[26] and Follansbee.[27] The given values are $p = 1/2$, $q = 3/2$, $g_0 = 0.8$, and $\dot{\varepsilon} = 10^{-4}$ s^{-1}. The work hardening $f(\varepsilon)$ was incorporated by taking a polynomial representation of the stress-strain curve for single crystals with the [001] and [$\bar{1}$34] orientations, as shown in Figure 15. This is the only manner by which the complex three-stage response can be incorporated without excessive complexity. The [001] orientation is expected to have the lowest threshold pressure for twinning of all orientations, whereas [$\bar{1}$34] should have a substantially higher threshold pressure due to its more gradual hardening. The polynomial used in these calculations is, for [001],

$$f(\varepsilon) = 45{,}510\varepsilon^6 - 86{,}899\varepsilon^5 + 63{,}406\varepsilon^4 - 21{,}834\varepsilon^3 + 2901.8\varepsilon^2 + 464.8\varepsilon^1 - 1.92 \qquad [7]$$

For [$\bar{1}$34],

$$f(\varepsilon) = -10{,}871\varepsilon^6 + 1431\varepsilon^5 - 7329\varepsilon^4 + 1690.3\varepsilon^3 + 126.8\varepsilon^2 - 2.34\varepsilon^1 + 0.07 \qquad [8]$$

The use of a polynomial to describe work hardening is a necessary assumption, because it is excessively difficult to model dislocation responses for monocrystals. The modified MTS constitutive equation was used to predict the response as a function of temperature and strain rate. The rationale

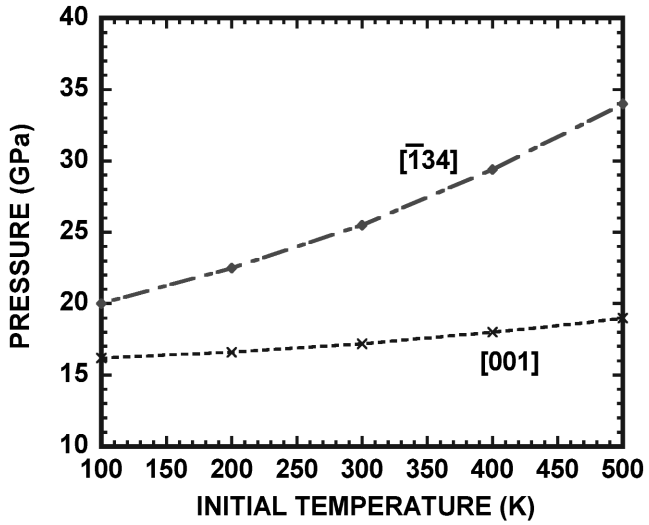

Fig. 16—Effect of temperature on the twinning threshold pressure for [001] and [$\bar{1}$34]. The orientation [$\bar{1}$34] shows a slightly higher temperature dependence.

described by Meyers *et al.*[28] was used to determine the threshold stress for twinning. The slip stress, σ_S, and twinning stress, σ_T, are set equal:

$$\sigma_S = \sigma_T \qquad [9]$$

The stress for twinning has an orientation dependence given in Table II.

By applying Eq. [9], in conjunction with Eqs. [2] through [6], we obtain the threshold for the two orientations: [001] (using Eq. [7]) and [$\bar{1}$34] (using Eq. [8]), assuming a grain size equal to the diameter of the shocked specimens (3 mm). The results for different initial temperatures are shown in Figure 16. The [$\bar{1}$34] orientation is affected by temperature to a larger extent than [001]. At ambient temperature, the [$\bar{1}$34] orientation has a threshold pressure of 25 GPa, whereas [001] has a threshold pressure of 17 GPa. This is the first calculation of the orientation dependence of threshold shock pressure for twinning.

V. CONCLUSIONS

The results obtained in this investigation are successfully interpreted in terms of crystallographic slip and mechanical twinning. For [001], the activation of eight slip systems simultaneously provides a higher work-hardening rate at the outset of plastic deformation. This results in higher dislocation densities and "tighter" cells. It also has a direct bearing on twinning. The orientation [$\bar{1}$34] has less symmetry and a much more gradual work-hardening curve correlating to lower dislocation densities and larger cell sizes. The results presented here confirm a recent investigation by Meyers *et al.*[5,6] There are two clear regimes of plastic deformation with different microstructural features: slip, dominated by dislocations organizing themselves into cells; and twinning/stacking faults, characterized by planar features. The orientation dependence of the threshold pressure for twinning cannot be explained by differences in Schmid factors alone. A constitutive procedure developed earlier[21] was applied to both [001] and [$\bar{1}$34], where slip and twinning are competing mechanisms.

The experimentally determined slip-twinning transition occurs for pressures that are orientation dependent: 20 to 40 GPa initial pressure for [001] and 40 to 60 GPa initial pressures for [$\bar{1}$34]. By using the simulated pressure profiles (Figure 4), more exact transition pressures can be defined. These values are higher than earlier results by DeAngelis and Cohen[15]: 14 GPa for [001] and 16 GPa for [111]. The transition pressures calculated (17 GPa for [001] and 25 GPa for [$\bar{1}$34]) are closer to the DeAngelis and Cohen results and suggest there could be a time dependence for twinning not considered in the computations. This time dependence seems to manifest itself in the submicrosecond regime imparted by the laser-induced shock and is consistent with a limiting velocity for twin propagation. This difference may also fit well with the experimental observation that in flyer plate experiments with longer pulse durations, dislocation densities are higher because of a longer dwell time. Because of the short pulse durations, the dislocation densities are lower, requiring a higher pressure to nucleate twinning. The calculated results are the first attempt to predict the orientation dependence of the twinning threshold. They qualitatively explain the difference encountered.

ACKNOWLEDGMENTS

This research is supported by the United States Department of Energy (Grant No. DE-FG03-98DP00212) and by the LLNL. The use of the University of Rochester OMEGA Laser Facility through the interaction of Dr. T. Boehly is gratefully acknowledged. The authors also thank the National Center for Electron Microscopy, Lawrence Berkeley National Laboratory, and Oak Ridge National Laboratory for use of their TEM facilities. The [$\bar{1}$34] crystal was provided by Prof. S.N. Monteiro.

REFERENCES

1. C.S. Smith: *Trans. AIME*, 1958, vol. 212, pp. 574-78.
2. Q. Johnson, A. Mitchell, R.N. Keeler, and L. Evans: *Phys. Rev. Lett.*, 1970, vol. 25, pp. 1109-11.
3. E. Zaretsky: *J. Appl. Phys.*, 1995, vol. 78, pp. 3740-47.
4. J.S. Wark, R.R. Whitlock, A.A. Hauer, J.E. Swain, and P.J. Solone: *Phys. Rev. B*, 1989, vol. 40, pp. 5705-14.
5. M.A. Meyers, F. Gregori, B.K. Kad, M.S. Schneider, D.H. Kalantar, B.A. Remington, J.S. Wark, T. Boehly, and G. Ravichandran: in *Shock Compression of Condensed Matter—2001*, M.D. Furnish, N.N. Thadhani, and Y. Horie, eds., AIP, New York, NY, 2002, pp. 619-22.
6. M.A. Meyers, F. Gregori, B.K. Kad, M.S. Schneider, D.H. Kalantar, B.A. Remington, G. Ravichandran, and T. Boehly: *Acta Mater.*, 2003, vol. 51, pp. 1211-28.
7. O. Johari and G. Thomas: *Acta Metal.*, 1964, vol. 12, pp. 1153-59.
8. L.E. Murr: in *Shock Waves and High-Strain-Rate Phenomena in Metals*, M.A. Meyers and L.E. Murr, eds., Plenum, New York, NY, 1981, pp. 607-73.
9. F.I. Grace: *J. Appl. Phys.*, 1969, vol. 40, pp. 2649-57.
10. G.T. Gray III: in *Shock-Wave and High-Strain-Rate Phenomena in Materials*, M.A. Meyers, L.E. Murr, and K.P. Staudhammer, eds., Marcel Dekker, New York, NY, 1992, pp. 899-902.
11. E. Hornbogen: *Acta Metal.*, 1962, vol. 10, pp. 978-86.
12. M.A. Meyers: *Scripta Metall.*, 1978, vol. 12, pp. 21-26.
13. J. Weertman: in *Shock Waves and High Strain Rate Phenomena in Metals*, M.A. Meyers and L.E. Murr, eds., Plenum Press, New York, NY, 1981, pp. 469-86.
14. M. Mogilevskii: *Phys. Rep.*, 1983, vol. 97, pp. 359-62.

15. R.J. De Angelis and J.B. Cohen: *J. Met*., 1963, vol. 15, pp. 681-87.
16. D.H. Kalantar, J. Belak, E. Bringa, K. Budil, M. Caturla, J. Colvin, M. Kumar, K.T. Lorenz, R.E. Rudd, J. Stolken, A.M. Allen, K. Rosolankova, J.S. Wark, M.A. Meyers, and M.S. Schneider: *Phys. Plasmas*, 2003, vol. 5, pp. 1569-76.
17. J. Lindl: *Phys. Plasmas*, 1995, vol. 2, pp. 3933-82.
18. R.L. Nolder and G. Thomas: *Acta Metall*., 1963, vol. 11, pp. 994-1001.
19. R.L. Nolder and G. Thomas: *Acta Metall*., 1964, vol. 12, pp. 227-40.
20. J. Diehl: *Z. Metallkd*., 1956, vol. 47, pp. 331-41.
21. L.E. Murr, M.A., Meyers, C.-S Niou, Y.-J Chen, S. Pappu, and C. Kennedy: *Acta Mater*., 1997, vol. 45, pp. 157-75.
22. M.A. Meyers, D.J. Benson, O. Voehringer, B.K. Kad, Q. Xue, and H.-H. Fu: *Mater. Sci. Eng*., 2002, vol. A322, pp. 194-216.
23. L.E. Murr: in *Shock Waves in Condensed Matter*, S.C. Schmid and N.C. Holmes, eds., Elsevier, Amsterdam, 1988, pp. 315-20.
24. J.W. Swegle and D.E. Grady: *J. Appl. Phys*., 1985, vol. 58, pp. 692-701.
25. M.A. Meyers: *Dynamic Behavior of Materials*, John Wiley, New York, NY, 1994, p. 150.
26. P.S. Follansbee and G.T. Gray III: *Mater. Sci. Eng*., 1991, vol. 138, pp. 23-31.
27. P.S. Follansbee: in *Metallurgical Applications of Shock-Wave and High-Strain Rate Phenomena*, L.E. Murr, K.P. Staudhammer, and M.A. Meyers, eds., Marcel Dekker, New York, NY, 1986, pp. 451-79.
28. M.A. Meyers, O. Voehringer, and V.A. Lubarda: *Acta Mater*., 2001, vol. 49, pp. 4025-39.